RSC Advances

PAPER

View Article Online
View Journal | View Issue

Cite this: *RSC Adv.*, 2025, **15**, 10602

Alkoxy-modified terpyridine complexes as efficient photocatalysts for diclofenac potassium degradation in pharmaceutical wastewater†

Ehsan Ullah Mughal, *[a] Nafeesa Naeem, [a] Farwa Zainab,[a] Ayesha Javaid,[b] Muhammad Imran,*[b] Sujeet Kumar Pandey,[c] Amina Sadiq,[d] Ayza Jabeen,[a] Hanan A. Ogaly,[e] Fatimah A. M. Al-Zahrani[e] and Abdullah Yahya Abdullah Alzahrani[f]

This study explores the synthesis and application of terpyridine-based metal complexes (**C1–C6**) for the degradation of diclofenac potassium (**DCF**), a widely used pharmaceutical pollutant. Terpyridine (TPY) ligands and their metal complexes were synthesized and characterized using FTIR, UV-Vis, ^{1}H NMR, ^{13}C NMR spectroscopy, and mass spectrometry. The novelty of this study lies in the fact that, for the first time, such structures were investigated/explored as potential photocatalysts for the degradation of **DCF**. The study demonstrates that the target complex compounds exhibit remarkable catalytic efficiency, facilitating the effective degradation of the target pollutant, **DCF**. The catalytic efficiency of the complexes (**C1–C6**) in the degradation process was investigated under optimized conditions, including pH and catalyst concentration. A detailed mechanistic study was conducted to elucidate the pathways involved in diclofenac degradation. Kinetic parameters were determined, demonstrating the reaction followed pseudo first-order kinetics. Furthermore, the recyclability of the TPY complexes was assessed over multiple degradation cycles, confirming their stability and reusability. Moreover, computational chemistry techniques utilizing density functional theory (DFT) efficiently explain the electrical properties of the target molecules. The molecular electrostatic potential (MEP) is a theoretical model widely utilized in catalyst chemistry to examine potential sites for nucleophilic and electrophilic attacks on photocatalysts and pollutants using a reactivity map. The density of states (DOS) indicated that **C5** exhibited enhanced photoactivity owing to the more prominent localization and delocalization of the highest occupied molecular orbital (HOMO) and lowest unoccupied molecular orbital (LUMO). The adsorption route of **DCF** on **C2**, **C4**, and **C5** was accurately predicted using molecular electrostatic potential (MEP) descriptors. This study highlights the potential of TPY-based catalysts as efficient and sustainable materials for the remediation of pharmaceutical contaminants in water systems. The enhanced photocatalytic performance is attributed to the optimized electronic structure and the strategic incorporation of alkoxy-functionalized TPY scaffolds. Compared to previous studies on methylene blue (MB) degradation, the newly synthesized complexes exhibit significantly higher efficiency, particularly in the degradation of **DCF**, demonstrating superior reaction kinetics and recyclability. These findings underscore their promise as next-generation photocatalysts for environmental applications.

Received 15th February 2025
Accepted 31st March 2025

DOI: 10.1039/d5ra01117e

rsc.li/rsc-advances

1. Introduction

Diclofenac potassium (**DCF**), a widely used non-steroidal anti-inflammatory drug (NSAID), is commonly prescribed for the treatment of pain, inflammation, and fever.[1] Due to its high solubility, rapid absorption, and therapeutic effectiveness, **DCF** has become an essential pharmaceutical for human and veterinary medicine.[2] However, the frequent and extensive use of **DCF** has led to its persistent release into aquatic environments through wastewater treatment plants, industrial discharges, and improper disposal of pharmaceuticals.[3–5]

---

[a] *Department of Chemistry, University of Gujrat, Gujrat-50700, Pakistan. E-mail: ehsan.ullah@uog.edu.pk*

[b] *School of Chemistry, University of the Punjab, Lahore, 54000, Pakistan. E-mail: imran.hons@pu.edu.pk*

[c] *Department of Chemical and Biochemical Engineering, Rajiv Gandhi Institute of Petroleum Technology, Jais, Amethi 229304, India*

[d] *Department of Chemistry, Govt. College Women University, Sialkot-51300, Pakistan*

[e] *Chemistry Department, College of Science, King Khalid University, Abha 61421, Saudi Arabia*

[f] *Department of Chemistry, Faculty of Science and Arts, King Khalid University, Mohail Assir, Saudi Arabia*

† Electronic supplementary information (ESI) available. See DOI: **https://doi.org/10.1039/d5ra01117e**

As an emerging pollutant, **DCF** is categorized under pharmaceutical contaminants that pose a serious threat to environmental health.[6] Conventional wastewater treatment systems are often insufficient for the complete removal of such organic micropollutants, resulting in their accumulation in water bodies.[7,8] Residues of **DCF** have been detected in surface water, groundwater, and even drinking water at trace levels, raising significant environmental and health concerns.[9]

The presence of **DCF** in aquatic systems is harmful to both aquatic life and human health.[10] Ecotoxicological studies have shown that even at low concentrations, **DCF** disrupts aquatic ecosystems by causing oxidative stress, endocrine disruption, and cellular damage in aquatic organisms such as fish and invertebrates.[11,12] Long-term exposure can lead to developmental abnormalities, reduced reproduction rates, and mortality in aquatic species.[13] Furthermore, its persistence in the environment contributes to bioaccumulation and biomagnification across the food chain, ultimately posing a risk to human health when contaminated water is consumed.[14,15]

To address this environmental challenge, the development of efficient and sustainable degradation methods is imperative. Among the strategies explored, photodegradation has emerged as a promising approach for the breakdown of pharmaceutical pollutants.[16] Photodegradation processes, facilitated by photocatalysts, leverage light energy to degrade complex organic molecules into less harmful byproducts.[17] Various materials have been explored for the degradation of diclofenac in recent years, including metal oxides, photocatalysts, carbon-based materials, and enzymatic systems.[18–21] These approaches have demonstrated varying degrees of success in breaking down the compound, with challenges such as incomplete degradation, formation of toxic by-products, and limited recyclability often reported.[22,23] Several materials have been studied for **DCF** degradation, each with distinct benefits and challenges. Titanium dioxide (TiO_2) photocatalysts are highly efficient under ultra violet (UV) light but exhibit limited activity in visible light and are prone to deactivation.[24] Carbon-based materials, such as graphene oxide and biochar, offer high adsorption capacity but are hindered by charge recombination and slow electron transfer.[25,26] Metal–organic frameworks (MOFs) show promising catalytic performance but face issues with structural instability in aqueous conditions.[27] Enzymatic methods using laccases and peroxidases provide eco-friendly alternatives but are constrained by high costs and enzyme instability.[28] These limitations emphasize the need for more durable and efficient catalytic systems for diclofenac removal from wastewater.[29,30]

Recent studies have highlighted the potential of coordination complexes as effective catalysts for pharmaceutical degradation.[31,32] Among these, TPY-based complexes have gained attention for their ability to facilitate redox reactions, promote selective degradation pathways, and exhibit remarkable recyclability.[33] In our earlier work, we successfully demonstrated the degradation of methylene blue using TPY metal complexes, revealing their robust catalytic efficiency and stability under diverse conditions.[34,35] In this context, the use of metal complexes has gained significant attention due to their unique electronic structures, stability, and ability to promote efficient photodegradation reactions.

TPY-based metal complexes (Fig. 1) have proven to be versatile compounds in catalysis and photodegradation studies.[36,37] TPYs, as polydentate ligands, exhibit excellent coordination ability with transition metals, forming stable complexes with tailored electronic properties.[38] These complexes often act as effective photosensitizers and photocatalysts under light irradiation, enabling the activation of molecular oxygen or generation of reactive oxygen species (ROS), which are crucial for the degradation of organic pollutants.[39,40] The tunability of TPY ligands and their corresponding metal complexes allows for enhanced photophysical properties, which can be optimized for specific environmental applications.[41,42]

Recent studies have highlighted the potential of TPY complexes in addressing environmental pollution through photodegradation mechanisms.[34,35] Their ability to degrade organic pollutants, such as dyes, pesticides, and pharmaceutical residues, has demonstrated significant advancements in pollutant removal efficiency, recyclability, and kinetics.[43] However, comprehensive studies focusing on the degradation of **DCF** using TPY-based systems remain limited, necessitating further investigation into their synthesis, mechanism, and practical applicability.

Inspired by these findings, the current study extends the application of these complexes to the degradation of **DCF**, aiming to establish a sustainable and effective method for its removal from water systems. This work contributes to advancing the field by exploring the catalytic potential of TPY complexes for addressing persistent pharmaceutical pollutants. This study aims to explore the application of TPY-based metal complexes for the photodegradation of **DCF**. The work focuses on the synthesis and characterization of the complexes, their photodegradation mechanisms, kinetics, and recyclability under environmentally relevant conditions. By addressing these aspects, the present study contributes to the development of efficient and sustainable approaches for the removal of pharmaceutical pollutants, offering a potential solution for

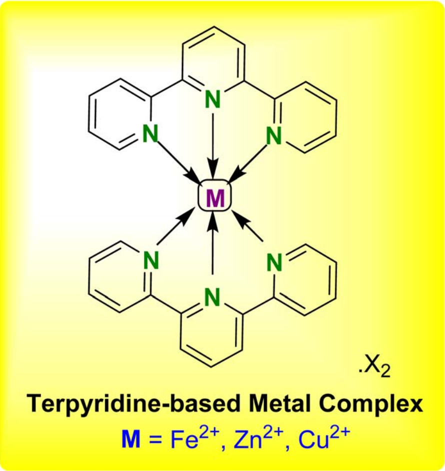

Fig. 1 General structure of TPY-based metal complex.

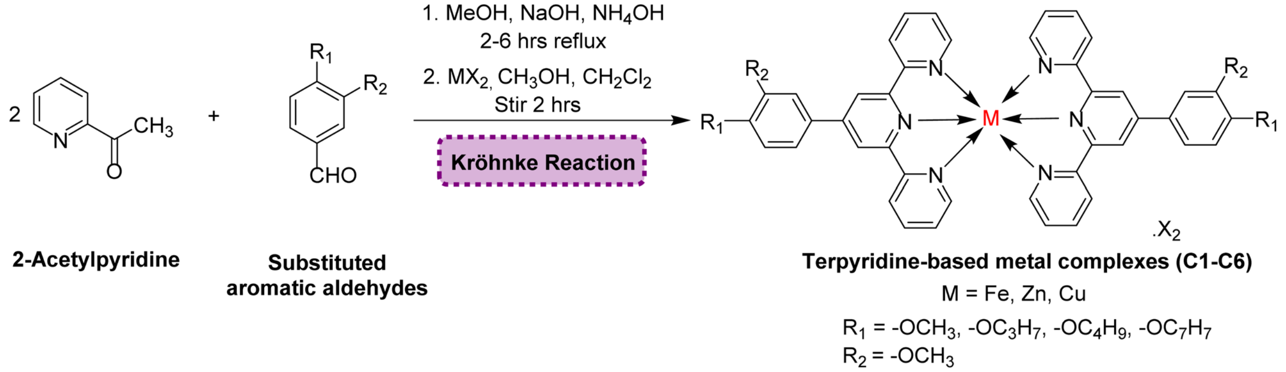

Scheme 1 Synthesis of TPY-based metal complexes (**C1–C6**).

mitigating environmental contamination caused by **DCF**. Furthermore, we have correlated our experimental photocatalytic degradation results with density functional theory (DFT) calculations. This computational analysis offered significant insights into the reaction mechanisms and provided an excellent agreement with the experimental data, reinforcing the reliability and efficiency of the proposed catalytic system. This integrative approach not only deepens the understanding of the degradation process but also demonstrates the potential of TPY complexes for broader environmental applications.

2. Materials and methods

2.1. Materials

All chemicals used in this study were purchased from established suppliers, including Merck and Sigma-Aldrich, and were utilized as received without any additional purification. Melting points were measured on an Electrothermal apparatus, and the values reported are uncorrected. Infrared (IR) spectra were recorded using a Bio-Rad spectrophotometer, and the results are expressed in wavenumber ($\bar{\upsilon}$) units. UV-Vis spectra were obtained using a Jasco V-660 UV-Vis spectrophotometer with quartz cells.

2.2. General procedure for the synthesis of ligands (L1–L4) and complexes (C1–C6)

The synthesis of TPY-based ligands and their corresponding metal complexes has been reported in our previous publication.[44]

2.3. Photocatalytic activity

The photocatalytic experiments were carried out for the removal of **DCF** using as-synthesized complexes as photocatalysts.[16] For a standard catalytic run, 10 mg of each catalyst was added to the 100 mL of a **DCF** solution (10 mg L^{-1}). The resulting suspension was placed in the dark for approximately half an hour under continuous magnetic stirring. A small aliquot of this suspension was withdrawn using a syringe fitter to remove any catalyst particles, and the absorbance was measured with a UV-Vis spectrophotometer at the maximum wavelength of 276 nm. According to Beer–Lambert law, this absorbance is proportional to the concentration and was considered the initial concentration (C_0) before light exposure. Subsequently, the suspension was irradiated using a 300 W xenon lamp as the light source. The aliquots were taken at 15 min intervals, their absorbance was recorded, and termed as **DCF** concentration C_t at certain time interval (t). In this way, the obtained data was used to calculate the photocatalytic efficiency using following equation (eqn (1)).

$$\text{Photocatalytic efficiency (\%)} = \frac{C_0 - C_t}{C_0} \times 100 \qquad (1)$$

In order to evaluate the impacts of three key parameters (initial concentration of **DCF**, photocatalyst loading, and pH of solution) on photocatalytic removal of **DCF**, the above-mentioned experiments were carried out by varying one parameter in certain range while keeping others constant. For instance, the initial concentration of **DCF** was varied from 5 mg L^{-1} to 25 mg L^{-1} while keeping constant catalyst loading of 10 mg and maintaining a pH of 7. The highest photocatalytic efficiency under specific reaction conditions denotes the optimized parameter. Therefore, for further experiments, the optimal **DCF** concentration of 10 mg L^{-1} was retained at neutral pH whereas the catalyst loading was varied from 10 mg to 60 mg. To study the effect of pH, the optimized **DCF** concentration and catalyst loading were maintained, and the pH was adjusted within the range of 3–9 using 0.1 M HCl and 0.1 M NaOH. Moreover, the relative influence of the main reactive species of the photocatalytic process was explored by conducting the photocatalytic experiments under optimized conditions in the presence of some scavenging species. Benzoquinone ($^{\bullet}O_2^-$scavenger) 2-propanol ($OH^{\bullet}$ scavenger), and triethanolamine (h^+ scavenger) were added (2 mL) in separate experiments and photocatalytic efficiency was determined.

2.4. Computational study

2.4.1 DFT study. DFT is used in all the calculations in the Gaussian 09 package.[45,46] Gauss View 6 software[47] is used for building molecular structures and results visualization. Here we use methods is B3LYP and the 3-21G basis set that are employed to calculate in order to identify the optimal theoretical method for the study of various compounds.

Computational chemistry methods employing DFT effectively elucidate the electrical characteristics of chemical compounds.[48] These techniques provide a deeper comprehension of the interactions between compounds and pollutants, hence enhancing the knowledge of the degradation mechanism and contributing to the creation of effective compounds. The electronic aspects of the compounds were computed using the Density of States (DOS) to examine the effects of compounds. DOS is an excellent tool for visually assessing the frontier molecular orbitals.[49]

3. Results and discussion

3.1. Chemistry

The TPY ligands and their metal complexes were synthesized according to established literature methods[44] (as outlined in Scheme 1 and Table 1). The characterization of ligands **L1–L4** and complexes **C1–C6** was performed using FTIR, UV-Vis, ^{1}H NMR, ^{13}C NMR spectroscopy, and mass spectrometry.

The spectral data of already reported compound **L4** is reported in the literature.[44] The spectroscopic data of all the newly synthesized ligands and complexes are given below.

3.1.1 4′-(4-Propoxyphenyl)-2,2′:6′,2″-terpyridine (L1). Off white crystalline solid; yield 78%; mp. 132–134 °C; UV λ_{max} ($CHCl_3$) = 284 nm; FTIR (cm^{-1}): 2958, 1631, 1534, 1239, 761, 681; ^{1}H NMR (500 MHz, DMSO-d_6): δ 8.78–8.76 (m, 2H, Ar–H), 8.68–8.66 (m, 4H, Ar–H), 8.06–8.03 (m, 2H, Ar–H), 7.90 (d, J = 10.0 Hz, 2H, Ar–H), 7.55–7.52 (m, 2H, Ar–H), 7.15 (d, J = 10.0 Hz, 2H, Ar–H), 4.03 (t, J = 10.0 Hz, 2H, $-\underline{OCH_2}CH_2CH_3$), 1.82–1.75 (m, 2H, $-OCH_2\underline{CH_2}CH_3$), 1.03 (t, J = 10.0 Hz, 3H, $-OCH_2CH_2\underline{CH_3}$); ^{13}C NMR (126 MHz, DMSO-d_6): δ 160.4, 156.0, 155.5, 149.8, 149.5, 138.0, 129.8, 128.6, 125.0, 121.4, 117.7, 115.7, 69.6, 22.5, 10.8; accurate mass (ESI) of $[M + H]^+$: calculated for $C_{24}H_{22}N_3O$ 368.1762; found 368.1753.

3.1.2 4′-(4-Butoxyphenyl)-2,2′:6′,2″-terpyridine (L2). Off-white amorphous solid, yield: 73%; mp. 162–164 °C; UV λ_{max} ($CHCl_3$) = 273 nm; FTIR (cm^{-1}): 2978, 1633, 1585, 1134, 1239, 673; ^{1}H NMR (600 MHz, DMSO-d_6): δ 8.77–8.76 (m, 2H, Ar–H), 8.68–8.65 (m, 4H, Ar–H), 8.05–8.03 (m, 2H, Ar–H), 7.91 (d, J = 10.0 Hz, 2H, Ar–H), 7.56–7.52 (m, 2H, Ar–H), 7.15 (d, J = 10.0 Hz, 2H, Ar–H), 4.02 (t, J = 10.0 Hz, 2H, $-\underline{OCH_2}CH_2CH_2CH_3$), 1.83–1.76 (m, 2H, $-OCH_2\underline{CH_2}CH_2CH_3$), 1.60–1.56 (m, 2H, $-OCH_2CH_2\underline{CH_2}CH_3$), 1.02 (t, J = 10.0 Hz, 3H, $-OCH_2CH_2CH_2\underline{CH_3}$); ^{13}C NMR (151 MHz, DMSO-d_6): δ 160.4, 156.1, 155.4, 149.8, 149.4, 138.1, 129.7, 128.5, 125.0, 121.4, 117.7, 115.6, 69.7, 31.1, 22.4, 10.8; accurate mass (ESI) of $[M + H]^+$: calculated for $C_{25}H_{24}N_3O$ 382.1919; found 380.1906.

3.1.3 4′-(4-(Benzyloxy)phenyl)-2,2′:6′,2″-terpyridine (L3). White crystalline solid; yield: 74%; mp. 155–157 °C; UV λ_{max} ($CHCl_3$) = 288 nm; FTIR (cm^{-1}): 2918, 1492, 1355, 1234, 982, 612; ^{1}H NMR (500 MHz, DMSO-d_6): δ 8.78–8.77 (m, 2H, Ar–H), 8.69–8.66 (m, 4H, Ar–H), 8.06–8.03 (m, 2H, Ar–H), 7.55–7.47 (m, 7H, Ar–H), 7.45–7.41 (m, 2H, Ar–H), 7.38–7.34 (m, 1H, Ar–H), 7.20–7.18 (m, 1H, Ar–H), 5.25 (s, 2H, $-OCH_2-$); ^{13}C NMR (126 MHz, DMSO-d_6): δ 159.5, 156.1, 155.4, 150.0, 149.8, 139.6, 138.0, 137.4, 131.0, 129.0, 128.38, 128.32, 125.0, 121.4, 120.0, 118.6, 116.4, 113.6, 69.8 (remaining carbons are isochronous); accurate mass (ESI) of $[M + H]^+$: calculated for $C_{28}H_{22}N_3O$ 416.1763; found 416.1760.

3.1.4 [Fe(4′-(4-propoxyphenyl)-2,2′:6′,2″-terpyridine)]$_2$·2PF$_6$ (C1). Dark purple amorphous solid; yield: 80%; mp. above 300 °C; UV λ_{max} (CH_3CN) = 289, 548 nm; FTIR (cm^{-1}): 1498, 1209, 1173, 931, 833, 565; ^{1}H NMR (600 MHz, acetone-d_6): δ 9.60 (s, 2H, Ar–H), 9.04 (d, J = 12.0 Hz, 2H, Ar–H), 8.81–8.76 (m, 1H, Ar–H), 8.47 (d, J = 12.0 Hz, 2H, Ar–H), 8.09–8.02 (m, 2H, Ar–H), 7.60 (d, J = 6.0 Hz, 2H, Ar–H), 7.37 (d, J = 6.0 Hz, 2H, Ar–H), 7.28–7.26 (m, 1H, Ar–H), 4.21–4.19 (m, 2H, $-\underline{OCH_2}CH_2CH_3$), 1.94–1.87 (m, 2H, $-OCH_2\underline{CH_2}CH_3$), 1.15 (t, J = 12.0 Hz, 3H, $-OCH_2CH_2\underline{CH_3}$); ^{13}C NMR (151 MHz, acetone-d_6): δ 161.7, 160.5, 158.5, 153.3, 150.1, 138.8, 129.3, 128.3, 128.2, 127.5, 124.0, 120.6, 115.53, 115.51, 69.6, 22.3, 9.9; accurate mass (ESI) of $[M + H]^+$: calculated for $C_{48}H_{43}FeN_6O_2$ 791.2797; found 791.2780.

3.1.5 [Zn(4′-(4-butoxyphenyl)-2,2′:6′,2″-terpyridine)]·SO$_4^{2-}$ (C2). Purple amorphous solid; yield: 74%; mp. above 300 °C; UV λ_{max} (CH_3CN) = 291, 575 nm; FTIR (cm^{-1}): 1598, 1338, 1255, 932, 822, 680; ^{1}H NMR (600 MHz, acetone-d_6): δ 9.36 (s, 2H, Ar–H), 9.04 (d, J = 12.0 Hz, 2H, Ar–H), 8.37–8.31 (m, 4H, Ar–H), 8.21 (d, J = 6.0 Hz, 2H, Ar–H), 7.57–7.55 (m, 2H, Ar–H), 7.31 (d, J = 12.0 Hz, 2H, Ar–H), 4.23 (t, J = 6.0 Hz, 2H, $-\underline{OCH_2}CH_2CH_2CH_3$), 1.89–1.84 (m, 2H, $-OCH_2\underline{CH_2}CH_2CH_3$), 1.61–1.55 (m, 2H, $-OCH_2CH_2\underline{CH_2}CH_3$), 1.05 (t, J = 6.0 Hz, 2H, $-OCH_2CH_2CH_2\underline{CH_3}$); ^{13}C NMR (151 MHz, acetone-d_6): δ 162.1, 156.0, 150.0, 148.4, 148.1, 141.3, 129.6, 127.7, 127.6, 123.3, 120.3, 115.4, 68.0, 31.1, 19.0, 13.2; accurate mass (ESI) of $[M + H]^+$: calculated for $C_{25}H_{24}N_3O_5SZn$ 542.0728; found 542.0720.

3.1.6 [Fe(4′-(4-(benzyloxy)phenyl)-2,2′:6′,2″-terpyridine)]$_2$·2PF$_6$ (C3). Brown amorphous solid; yield: 80%; mp. above 300 ° C; UV λ_{max} (CH_3CN) = 274, 562 nm; FTIR (cm^{-1}): 2925, 1589, 1420, 1230, 826, 550; accurate mass (ESI) of $[M + H]^+$: calculated for $C_{56}H_{43}FeN_6O_2$ 887.2797; found 887.2780.

3.1.7 [Zn(4′-(4-(benzyloxy)phenyl)-2,2′:6′,2″-terpyridine)]·SO$_4^{2-}$ (C4). Pale-yellow amorphous solid; yield: 79%; mp. above 300 °C; UV λ_{max} (CH_3CN) = 271, 573 nm; FTIR (cm^{-1}): 2912, 1593, 1365, 1240, 819, 539; accurate mass (ESI) of $[M + H]^+$: calculated for $C_{28}H_{22}N_3O_5SZn$ 576.0572; found 576.0561.

3.1.8 [Zn(4′-(4-propoxyphenyl)-2,2′:6′,2″-terpyridine)]·SO$_4^{2-}$ (C5). Purple amorphous solid; yield: 76%; mp. above 300 °C; UV λ_{max} (CH_3CN) = 289, 588 nm; FTIR (cm^{-1}): 2155, 1600, 1499, 1334, 1204, 552; ^{1}H NMR (500 MHz, DMSO-d_6): δ 9.34 (s, 2H, Ar–H), 9.16 (d, J = 10.0 Hz, 2H, Ar–H), 8.46 (d, J = 5.0 Hz, 2H, Ar–H), 8.31–8.26 (m, 2H, Ar–H), 7.96 (d, J = 5.0 Hz, 2H, Ar–H), 7.51–7.48 (m, 2H, Ar–H), 7.32 (d, J = 6.0 Hz, 2H, Ar–H), 4.16 (t, J = 10.0 Hz, 2H, $-\underline{OCH_2}CH_2CH_3$), 1.88–1.81 (m, 2H, $-OCH_2\underline{CH_2}CH_3$), 1.08 (t, J = 10.0 Hz, 3H, $-OCH_2CH_2\underline{CH_3}$); ^{13}C NMR (126 MHz, DEPT, DMSO-d_6): δ 148.2, 141.7, 135.3, 130.3, 130.2, 128.0, 124.0, 120.4, 115.7, 69.8, 22.5, 11.0; accurate mass (ESI) of $[M + H]^+$: calculated for $C_{24}H_{22}N_3O_5SZn$ 528.0572; found 528.0554.

3.1.9 [Cu(4′-(3,4-(dimethoxy)phenyl)-2,2′:6′,2″-terpyridine)]$_2$.2PF$_6$ (C6). Light green amorphous solid; yield: 84%; mp. above 300 °C; UV λ_{max} (CH_3CN) = 295, 589 nm; FTIR (cm^{-1}): 2915, 1630, 1300, 1000, 800, 550; accurate mass (ESI) of $[M + H]^+$: calculated for $C_{46}H_{39}CuN_6O_4$ 802.2329; found 802.2312.

Table 1 Chemical structures of TPY ligands (**L1–L4**) and metal complexes (**C1–C6**)

Compound no.	Chemical structure
L1	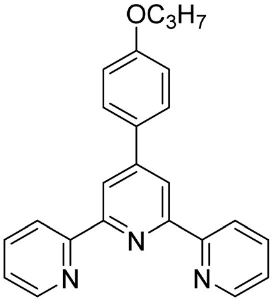
L2	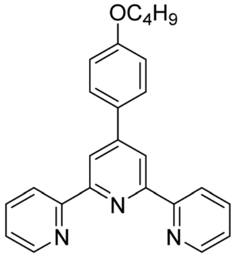
L3	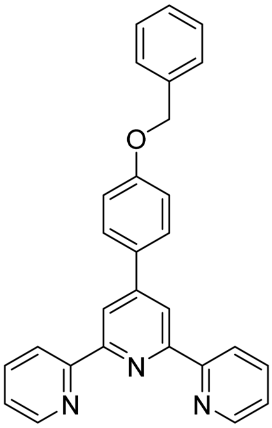
L4	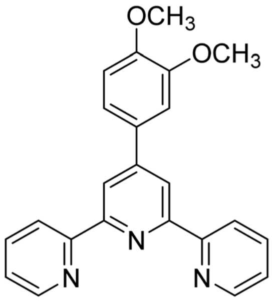
C1	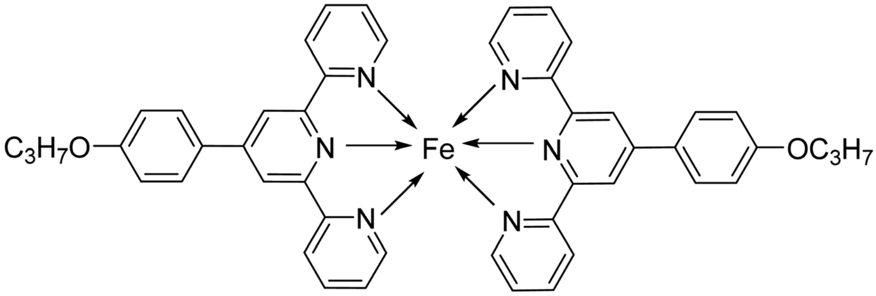

Table 1 (*Contd.*)

Compound no.	Chemical structure
C2	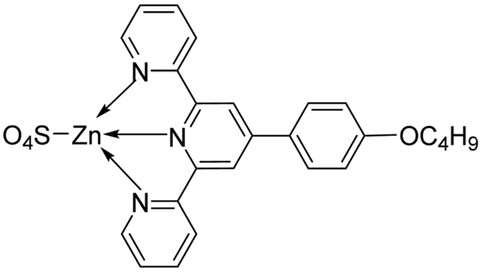
C3	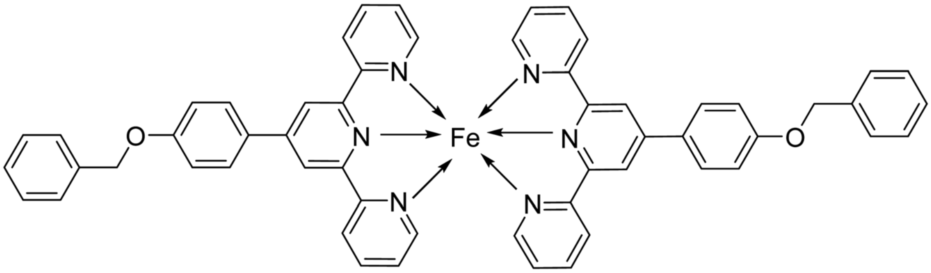
C4	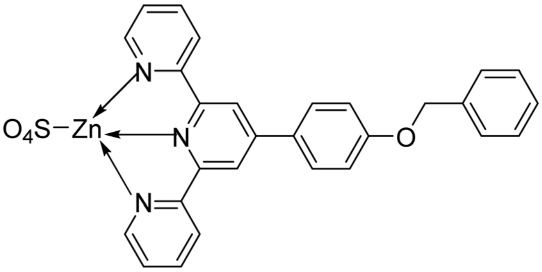
C5	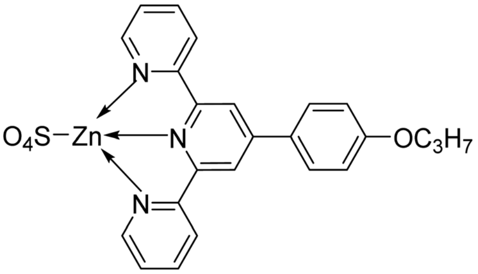
C6	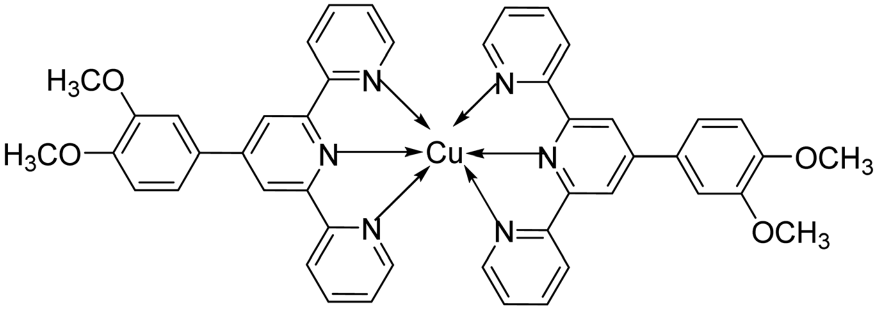

3.2. Photocatalytic activity

The photocatalytic capability of synthesized complexes was evaluated to catalyze the removal of **DCF** in aqueous media (Fig. 2). Initially, the **DCF** degradation without any catalyst and utilizing light irradiation alone was carried out as a blank experiment. It was noticed that degradation (2.77%) of **DCF** was negligible in the absence of the catalyst revealing that photolysis is insufficient for the **DCF** removal. Similarly, additional

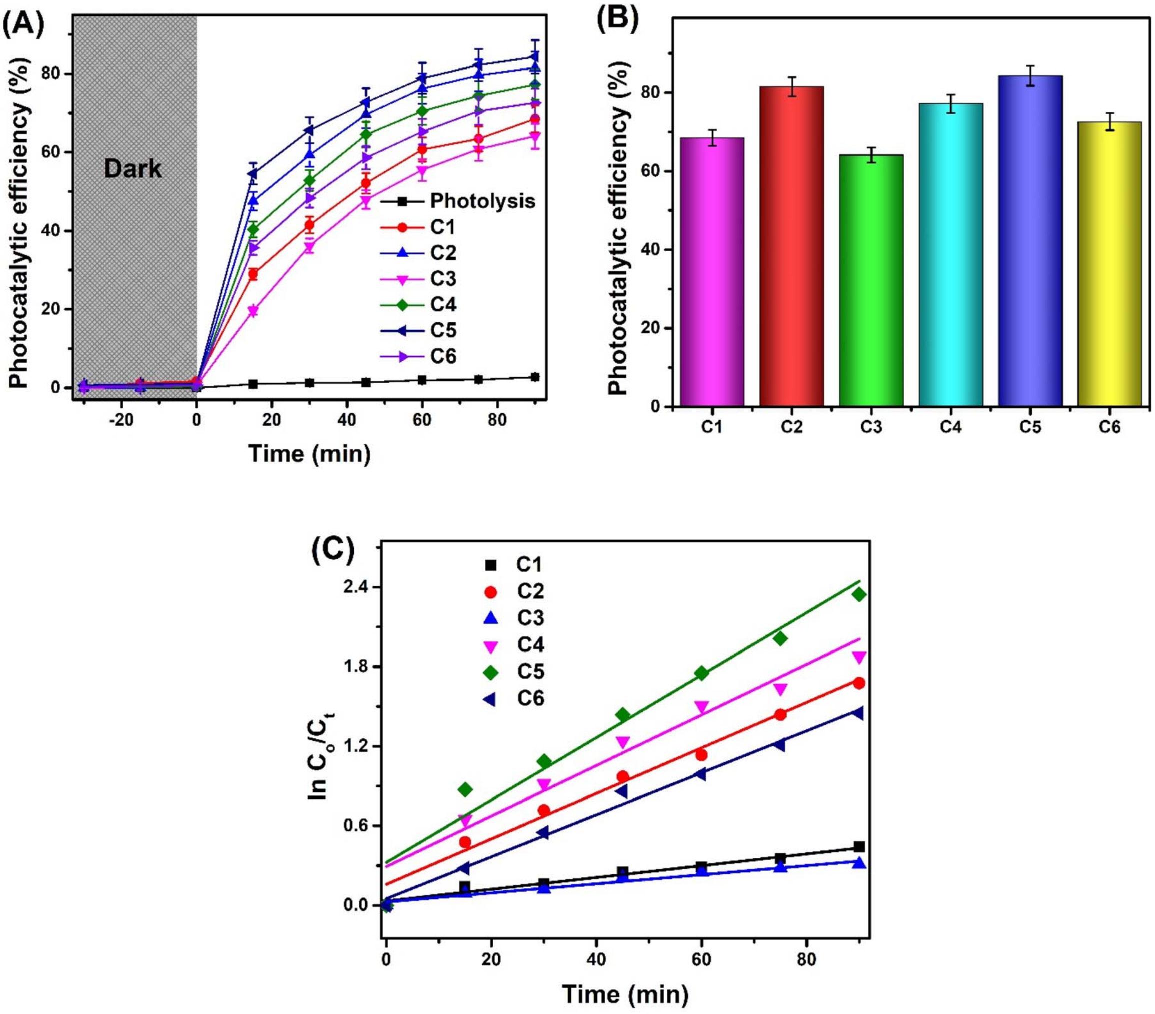

Fig. 2 (A) Photocatalytic efficiency of a synthesized complexes for the removal of DCF as a function of light irradiation time, (B) comparative photocatalytic efficiency, and (C) reaction kinetics of synthesized complexes.

control experiments were employed under dark conditions containing synthesized complexes only. No considerable change in degradation efficiency was observed in these experiments, indicating that the complexes exhibited minimal catalytic activity and only slight adsorptive behavior. This emphasizes the necessity of both light and the catalyst working together to achieve effective removal of **DCF**. Upon light irradiation, the photocatalytic efficiency boosted to a greater extent due to the synergistic role of light and the catalysts, facilitating the degradation of **DCF**. Fig. 2(A) shows that there is an abrupt enhancement in the degradation efficiency during the initial 15 to 30 min of irradiation, ascribed to the abundance of available catalytic sites at the start of the reaction. As reaction proceeds further, there is only a nominal increase in degradation efficiency and ultimately became almost constant between 75 to 90 min of light exposure. The occupation of maximum catalytic sites with **DCF** molecules at this stage of reaction were responsible for this behavior. It can be explained by the saturation of catalytic sites with **DCF** molecules, reducing the availability of free sites for further degradation. Additionally, the accumulation of reaction intermediates or byproducts on the catalyst surface could hinder the accessibility of fresh **DCF** molecules to the active sites.[50] When photocatalytic activity of synthesized complexes was compared among themselves, it was found that photocatalytic process is structural dependent where nature of central metal, type of ligand, and geometry attained by the metal complex play a crucial role. The observed degradation efficiencies for synthesized complexes were in the order: **C5** (84.3%) > **C2** (81.5%) > **C4** (77.2%) > **C6** (72.6%) > **C1** (68.5%) > **C3** (64.1%) (Fig. 2(B)). The highest degradation efficiency of **C5** is due to the small steric hindrance of propoxy group attached to the phenyl ring, which facilitates easier access of substrate molecules towards zinc metal centre. Moreover, the propoxy group, being a strong electron-donating group, stabilizes the Zn–ligand bond and enhances the catalytic capability of the zinc center. In case of **C2**, the photocatalytic efficiency slightly decreased because the butoxy group introduces greater steric hindrance compared to the propoxy group. The longer chain length of the butoxy group also weakens the Zn–ligand interaction, affecting charge transfer tendency of the complex. The

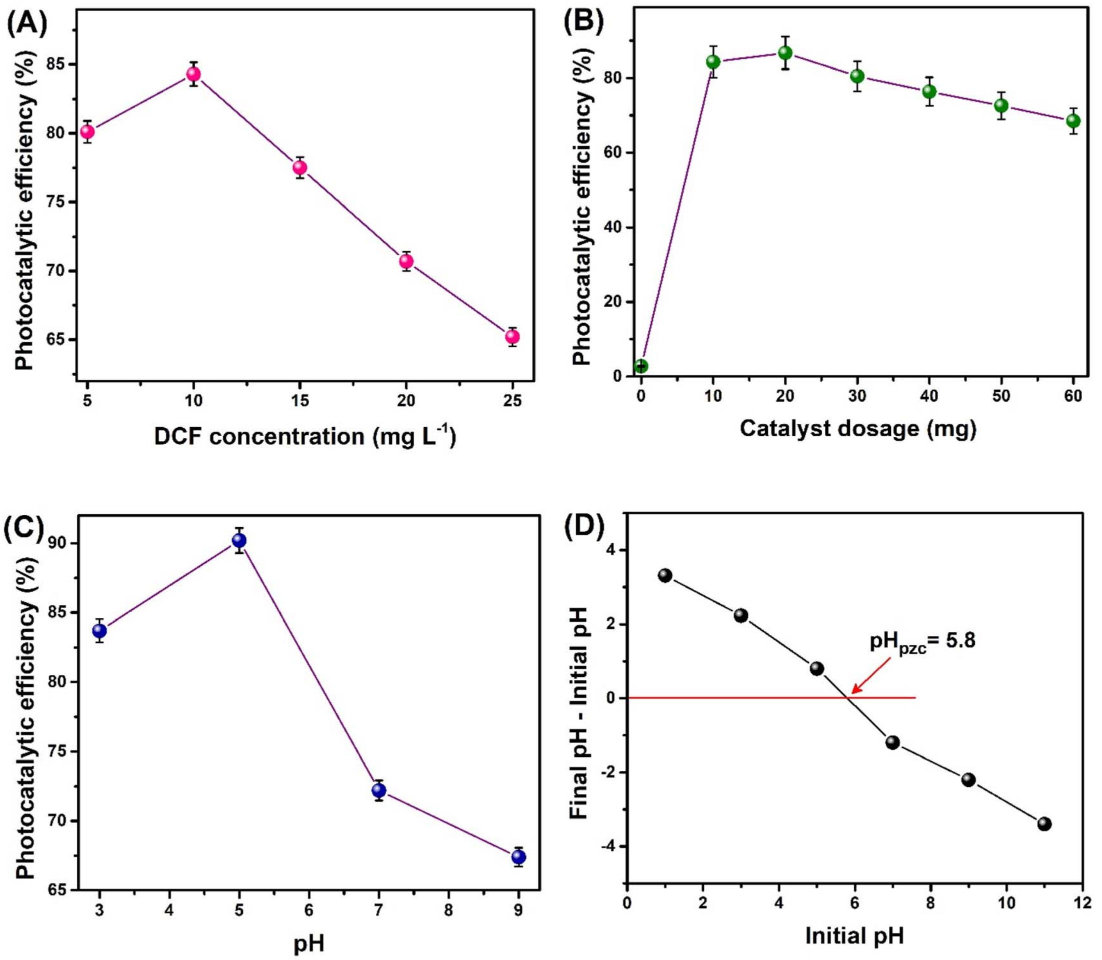

Fig. 3 Effect of operational parameters on the photocatalytic degradation of **DCF** under visible light irradiation using **C5** as photocatalyst: (A) **DCF** initial concentration, (B) catalyst dosage, (C) solution pH and (D) plot of change in pH *vs.* initial pH for the determination of pH_{pzc} of **C5** (intercept = pH_{pzc}).

presence of benzyloxy group in **C4** further reduced the degradation efficiency attributed to significant steric hindrance caused by the bulky benzene ring.[37] This bulkiness restricts substrate access to the Zn center, thus reducing catalytic efficiency. Although the benzyloxy group is an excellent electron-donor, it is less effective than alkoxy groups because of extensive delocalization over the aromatic ring. This phenomenon leads to reduced activation of the catalytic center. The superior performance of the zinc complexes is also attributed to their coordination number of 4, which allows maximum interaction with drug molecules as the zinc centre retains vacant sites for pollutant interaction.[35] Moreover, the stable d^{10} configuration of Zn^{2+} and its resulting redox inertness contribute to the stability of the complex[51] which may help to maintain an active substrate–host interaction for catalytic activity. This stability could also refrain the metal complex from participating in side-reactions or decompositions, allowing catalytic action only.

Among the remaining complexes, the Cu complex (**C6**) demonstrated better performance than the Fe complexes (**C1** and **C3**). The lower catalytic activity of Cu and Fe complexes compared to Zn complexes is primarily due to their coordination number of 6, forming an octahedral geometry where all sites are fully occupied by ligands.[36,52] This structure limits the exposure of the metal center to pollutant molecules, thereby reducing charge transfer between metal and ligand. Although both copper and iron complexes have similar coordination number, the ligand environment significantly influences photocatalytic performance. In **C6**, the ligand has dimethoxy groups that are relatively small, with less steric hindrance compared to the bulky ligands in **C1** and **C3**. Furthermore, the dimethoxy groups exhibit strong electron-donating capabilities due to their inductive and resonance effects, facilitating efficient electron transfer from the ligand to the metal center. In case of **C1** and **C3**, steric effects of the ligands also contribute to the diminished catalytic activity of Fe complexes. Despite the similar co-ordination number of Fe and Cu, the slightly higher catalytic efficiency of Cu complexes could be attributed to its higher intrinsic Lewis acidity[53] which could facilitate effective adsorption of substrate molecules onto the metal complex surface, initiating catalytic action.[54] Moreover, Lewis acidity is also associated with the separation of photoinduced electron–hole pairs, suppressing their recombination rate.[55]

3.3. DCF photodegradation kinetics

Kinetic study of the photocatalytic process is essential for understanding the pathway by which the substrate interacts with the catalyst and it helps to determine the reaction rate constant. The Langmuir–Hinshelwood kinetic model, modified to the pseudo first-order kinetics, is commonly applied to describe the degradation of organic contaminants.[56] The experimental data of photocatalytic reaction fitted well to the pseudo first-order kinetic model equation (eqn (2)) followed by the determination of rate constants from the slope of the plot between time and $\ln C_0/C_t$ (Fig. 2(C)).

$$\ln\frac{C_0}{C_t} = kt \tag{2}$$

The obtained values of k for **C1**, **C2**, **C3**, **C4**, **C5**, and **C6** were 0.00445 min^{-1}, 0.01716 min^{-1}, 0.00343 min^{-1}, 0.01907 min^{-1}, 0.02355 min^{-1}, and 0.01583 min^{-1}, respectively. The highest rate constants of Zn complexes (**C2**, **C4**, **C5**) among all the synthesized complexes were in agreement with their photocatalytic efficiencies indicating fast reaction kinetics of **DCF** degradation in the presence of these complexes.

In photocatalytic process, electric energy consumption helps to estimate operating costs and can be evaluated using "electric energy per order" (EEO) for a pseudo first-order kinetic reaction. The EEO can be calculated from the following equation (eqn (3)).

$$\text{EEO} = \frac{38.4 \times P}{V \times k} \tag{3}$$

where, P is the input power (kW) to the catalytic system, V is the solution volume (L) in the reactor, and k is the pseudo first-order reaction rate constant (min^{-1}).[57] The electrical energy required by the TPY-based complexes for the removal of **DCF** were 25887.64, 6713.28, 33586.01, 6040.90, 4891.72, and 7277.32 kW h per m^3 per order, for **C1**, **C2**, **C3**, **C4**, **C5**, and **C6**, respectively. Among all the synthesized composites, **C5** consumed the least energy during **DCF** removal. In the literature, EEO values ranging from 753.4 to 61, 538.5 kW h per m^3 per order have been reported for the removal of different pharmaceuticals[58] indicating that pharmaceutical degradation typically requires high energy consumption. However, in this study, the EEO values of all the synthesized complexes fall within the lower limit of this range. This is a significant consideration for evaluating treatment costs in the industrial applications, as electric energy can constitute a major fraction of the overall operating costs.

3.4. Operational parameters affecting photodegradation process

It has been known that operating conditions of pollutant concentration, catalyst dosage, and solution pH influence the photocatalytic efficiency, therefore, these parameters were studied in a specific range to determine optimal conditions. The photocatalyst (**C5**) with highest degradation efficiency was employed for further optimization studies.

3.4.1 Effect of primary drug concentration. The concentration of diclofenac may vary widely in real waste water effluents, therefore, photodegradation of diclofenac was studied by varying its concentration in the range of 5 mg L^{-1} to 25 mg L^{-1}, while keeping other parameters constant. Fig. 3(A) shows that degradation efficiencies of 80.1%, 84.3%, 77.5%, 70.7%, and 65.2% were obtained at 5 mg L^{-1}, 10 mg L^{-1}, 15 mg L^{-1}, 20 mg L^{-1}, and 25 mg L^{-1}, respectively. Formerly, an increase in degradation efficiency was observed with increasing drug concentration attributed to the surplus availability of catalytic sites relative to the drug molecules. Later, at higher concentrations, the drug molecules could not compete with the catalytic sites which were already occupied by other drug molecules. The photogenerated reactive species also became insufficient to degrade the excess diclofenac molecules, leading to a reduction in degradation efficiency at higher drug concentrations.[59]

3.4.2 Effect of catalyst loading. The photocatalytic removal of pollutants is greatly affected by the photocatalyst dosage. An optimal loading of photocatalyst ensures maximum degradation efficiency. To determine this, several photodegradation reactions were conducted at varying catalyst loadings (10 mg – 60 mg). Fig. 3(B) shows that the degradation efficiency initially increased by increasing amount of the catalyst. For instance, 84.3% degradation was observed at 10 mg, which further improved to 86.7% at 20 mg. The increased catalyst loading enhances number of active sites on the catalyst's surface, where pollutant molecules can adhere and reactive species are generated to facilitate pollutant degradation.[60] However, at relatively higher catalyst loadings (30 mg and beyond), a continuous decline in degradation efficiency was observed, reaching 68.5% at the highest catalyst loading of 60 mg. This decline can be attributed to several factors. Excessive catalyst concentration leads to agglomeration, reducing the availability of active sites. Moreover, the abundance of catalyst particles renders the drug solution turbid, hindering effective light absorption. This, in turn, affects the generation of reactive species necessary for catalytic action.[61] These factors collectively contribute to the reduced efficiency at higher catalyst dosages. Based on these observations, 20 mg was determined to be the optimal dosage for further studies.

3.4.3 Effect of reaction pH. The influence of pH on **DCF** degradation was investigated across a range of 3 to 9 under light irradiation, with the initial concentration of **DCF** fixed at 10 mg L^{-1}. As shown in Fig. 3(C), the degradation efficiency increased under mildly acidic conditions, followed by a significant drop as the pH increased. This behavior aligns with previous studies reported by Rueda-Salaya *et al.*[62] To better understand this trend, two key factors must be considered: the $\text{p}K_\text{a}$ of **DCF** and the point of zero charge (pH_pzc) of the catalyst. According to the literature, the $\text{p}K_\text{a}$ of diclofenac is 4.15 [63] whereas pH_pzc of the catalyst was experimentally determined to be 5.8 (Fig. 3(D)). In fact, these two important considerations (pH_pzc of the catalyst and $\text{p}K_\text{a}$ of the **DCF**) helped to select the pH range to be studied and the pH value at which maximum

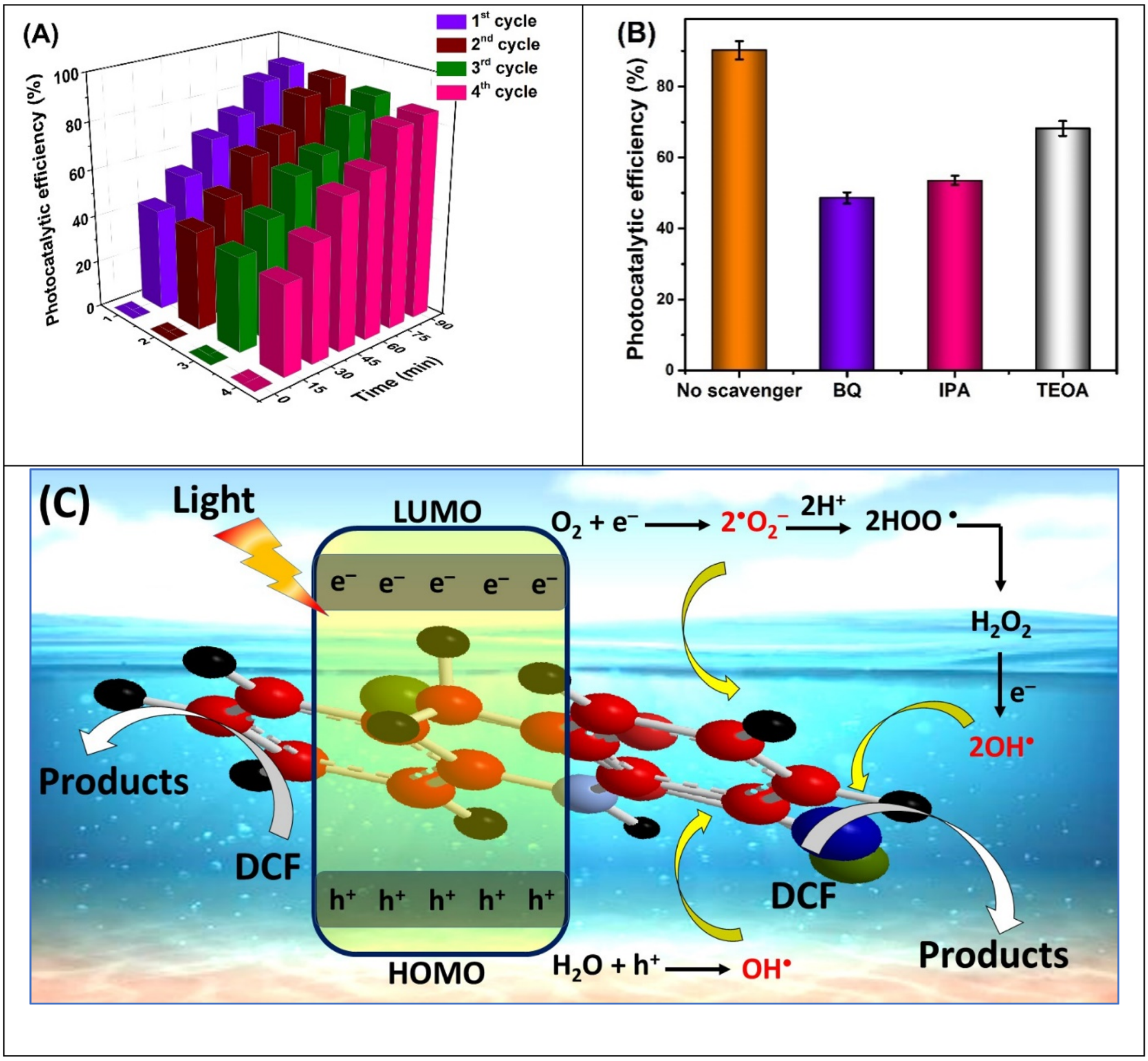

Fig. 4 (A) Reusability, (B) photocatalytic experiments in the presence of scavengers, and (C) plausible **DCF** degradation mechanism employing **C5** as photocatalyst under optimized conditions.

degradation efficiency was obtained was considered as optimum pH. Initially, in highly acidic conditions (pH = 3), where $pK_a > pH < pH_{pzc}$, both the drug and the catalyst are positively charged. This results in electrostatic repulsion between the two surfaces, thereby limiting the adsorption of the drug onto the catalyst surface, a prerequisite for catalytic action. The mild acidic (pH = 5) conditions favored this adsorption because at this pH **DCF** begins to deprotonate and acquires a negative charge, which attracts the positively charged catalyst surface. However, as the pH increases further (pH = 7), the catalyst surface also becomes negatively charged since this pH is higher than the pH_{pzc}. Consequently, electrostatic repulsion between the negatively charged **DCF** and the catalyst surface starts to dominate, reducing the degradation efficiency. At even higher pH values (pH = 9), this repulsion intensifies because the negative charge on **DCF** increases due to its complete deprotonation, further limiting its adsorption onto the catalyst surface.[64] The study of pH parameter highlights its critical role in determining the surface charge characteristics of both the drug and the catalyst, emphasizing the importance of optimizing pH conditions to achieve maximum photocatalytic performance.

3.5. Photocatalyst reusability

Reusability of a photocatalyst without significant loss in catalytic efficiency ensures sustainability, cost-effectiveness, and practical applicability of the material. The stability of **C5** was assessed by reusing the immobilized catalyst under optimal conditions in subsequent runs following the initial standard run. The experimental results demonstrated that the photocatalytic performance retains satisfactory reusability for up to four cycles (Fig. 4(A)). The observed degradation efficiencies were 90.2%, 89.7%, 88.0%, and 86.5% at 1st, 2nd, 3rd, and 4th catalytic runs, respectively. The slight reduced activity observed during the 4th cycle could potentially be attributed to the

Table 2 A comparative photocatalytic efficiency of **C5** for **DCF** removal[a]

Photocatalyst	DCF concentration	Catalyst loading	Source of light	Degradation efficiency (%)	Rate constant (min^{-1})	Reference
g-C_3N_4/NH_2-MIL-125	10 mg L^{-1}	250 mg L^{-1}	UV LED	100% in 2 h	0.0282	70
MIL-88 (Fe)/Ag_3PO_4/GCN	5 mg L^{-1}	0.5 g	300 W xenon lamp	>90% in 120 min	0.076	71
ZnO-CBS-Ni complex	50 mg L^{-1}	50 mg L^{-1}	Visible light	93% in 180 min	—	72
O-g-C_3N_4/ZnO/TiO_2@ halloysite nanotubes	10 mg L^{-1}	1.0 g L^{-1}	15 W UVA lamp	100% in 50 min	0.060	73
Cu_2ZnSnS_4	10 mg L^{-1}	1.0 g L^{-1}	300 W xenon lamp	90% in 120 min	—	74
C5	10 mg L^{-1}	20 mg	300 W xenon lamp	90.2% in 90 min	0.02355	This work

[a] CBS: Chitosan Boc-serine.

accumulation of intermediate compounds adsorbed on the surface of the photocatalyst.[65] Overall, minor catalytic loss (3.7%) over repeated runs suggests the scalable operational efficiency of **C5**.

3.6. Trapping experiments and reaction mechanism

The reactive oxygen species (ROS) generated at the catalyst surface upon light irradiation play a crucial role in the degradation process. To determine the contribution of these species, trapping experiments were conducted, where photocatalytic activity was evaluated in the presence of scavenging agents. A scavenging agent has a tendency to quench specific reactive species; therefore, when added to a photocatalytic reaction, it inhibits the activity due to the reduced availability of reactive species. The extent of reduction in photocatalytic efficiency in the presence of a specific scavenger correlates with the dominant role of that species in driving the degradation process. In this study, various scavenging agents were employed to validate the role of ROS (Fig. 4(B)). For instance, benzoquinone (BQ), a quencher for $^{\bullet}O_2^-$, was used to confirm its presence in the degradation mechanism. The significant suppression of **DCF** removal efficiency (48.6%) in the presence of BQ indicates that $^{\bullet}O_2^-$ was actively generated throughout the process, and played a key role in the degradation activity.[66] Similarly, 2-propanol (iso-propanol, IPA) was employed as a scavenger for hydroxyl radicals ($OH^{\bullet}$). The degradation of **DCF** was significantly inhibited (53.5%) in the presence of 2-propanol indicating that $OH^{\bullet}$ was also essential for **DCF** removal processes. Additionally, photoinduced holes (h^+) are generated simultaneously during the reaction. To investigate their contribution, triethanolamine (TEOA) was used as a scavenger in the aqueous solution.[67] A slight reduction in the degradation efficiency of **DCF** (68.2%) was observed, suggesting a limited contribution of holes to the photodegradation process. Based on these findings, a probable reaction mechanism is proposed to explain the involvement of these photoinduced species (Fig. 4(C)). The electrons in the highest occupied molecular orbital (HOMO) of **C5** are excited to lowest unoccupied molecular orbital (LUMO) upon absorbing energy from the incident photons. As a result, LUMO becomes electron-rich, whereas positive vacancies known as holes are left behind in the HOMO and it becomes electron-deficient.[68] The electrons present in LUMO reduce adsorbed oxygen molecules into superoxide anions which further react with nearby water molecules converting them into hydroperoxyl ($OOH^{\bullet}$) radicals, eventually converting into hydroxyl radicals ($OH^{\bullet}$).[69] In parallel, some hydroxyl radicals are directly generated through the oxidation of water molecules by the holes in the HOMO. These reactive species ($^{\bullet}O_2^-$ and $OH^{\bullet}$), being highly unstable and short-lived, attack the **DCF** molecules, breaking them down into simpler compounds through a series of steps.

3.7. Performance comparison of C5 with other photocatalysts

Table 2 provides a comparative analysis of the photodegradation efficiency of **C5** for **DCF** removal, benchmarked against other materials previously reported for the same application. A comprehensive literature scan indicates a notable gap in the use of coordination polymers and metal complexes specifically for **DCF** removal. To address this, the comparison incorporates a diverse range of materials, reported for similar studies. The results highlight the superior performance of our fabricated **C5** complex. Notably, **C5** achieves exceptional photocatalytic efficiency for **DCF** removal under visible light irradiation in the shortest time span, underscoring its potential as a highly effective and practical material for wastewater remediation applications.

3.8. Comparative performance evaluation of complexes based on the same TPY scaffold for methylene blue dye and diclofenac potassium degradation

The synthesized terpyridine-based metal complexes (**C1–C6**) were employed as heterogeneous photocatalysts for the degradation of **DCF**, a pharmaceutical pollutant. The photocatalytic efficiency of the complexes followed the order: **C5** (84.3%) > **C2** (81.5%) > **C4** (77.2%) > **C6** (72.6%) > **C1** (68.5%) > **C3** (64.1%). Among these, **C5** demonstrated the highest degradation efficiency, effectively removing 10 mg L^{-1} of **DCF** with a remarkable 90.2% degradation rate within 90 minutes under light irradiation, utilizing only 20 mg of catalyst at pH 5. The degradation kinetics conformed to the pseudo-first-order model, with the highest rate constant observed for **C5** (0.02355 per min) (Table 3).

A comparative analysis with our previously published studies on methylene blue (MB) degradation highlights the superior

Table 3 A comparative photocatalytic performance of TPY-based metal complexes in the degradation of methylene blue (MB) dye and diclofenac potassium (**DCF**)

Photocatalyst	**DCF** concentration	MB dye concentration	Catalyst loading	Source of light	Degradation efficiency (%)	Rate constant (min^{-1})	Reference
Complex **1** [Zn(4′-(4-methylphenyl)-2,2′:6′,2″-terpyridine)$(SO_4)^{2-}$]	—	10 mg L^{-1}	20 mg	18 W UV lamp	67.31% in 40 min	0.0099	35
Complex **7** [Zn(*N*,*N*-diphenyl-4-(2,2′:6′,2″-terpyridin-4′-yl) aniline)$(SO_4)^{2-}$]	—	10 mg L^{-1}	20 mg	18 W UV lamp	65.91% in 40 min	0.0110	35
Complex **5** [Zn (3,4-dimethoxyphenyl-2,2′:6′,2″-terpyridine)$(SO_4)^{2-}$]	—	15 mg L^{-1}	10 mg	UV lamp	79.84 in 120 min	0.009	34
Complex **C5** [Zn(4′-(4-propoxyphenyl)-2,2′:6′,2″-terpyridine)$SO_4{}^{2-}$]	10 mg L^{-1}	—	20 mg	300 W xenon lamp	90.2% in 90 min	0.02355	This work

efficiency of the newly synthesized complexes. In our earlier work, Fe(II), Co(II), and Zn(II) terpyridine complexes exhibited significant photocatalytic potential against MB degradation. Zinc-based complexes, particularly Complex **1** (67.31%) and Complex **7** (65.91%), showed the highest degradation efficiencies under optimized conditions (10 mg L^{-1} dye concentration, 20 mg catalyst dose, pH 4, 40 min irradiation time). The rate constants for these complexes were 0.009 min^{-1} and 0.011 min^{-1}, respectively, both following pseudo-first-order kinetics. Reusability tests revealed minimal loss of activity (8.62% and 7.01% over four cycles), indicating their sustainability in wastewater treatment applications[35] (Table 3).

Similarly, in another study from our group, the series **C1–C6** exhibited varying degradation efficiencies against MB, with **C5** achieving the highest efficiency (79.84%) and a rate constant of 0.009 min^{-1}. Zn-based complexes consistently outperformed their Fe-based counterparts despite having the same ligands, suggesting that the metal center significantly influences catalytic activity. The excellent recyclability of these catalysts further emphasized their practicality for long-term use in environmental remediation[34] (Table 3).

Compared to our previous research (Table 3),[34,35] the present study demonstrates significantly enhanced photocatalytic efficiency, particularly in the degradation of **DCF**. Complex **C5** not only outperformed its counterparts in degrading **DCF** (90.2% efficiency with a rate constant of 0.02355 min^{-1}) but also exhibited a remarkable improvement over the best-performing complexes from the MB studies. The increased efficiency can be attributed to the optimized electronic structure, which facilitates better charge transfer, enhanced generation of reactive oxygen species, and improved stability during repeated use. The incorporation of alkoxy (–OR) substituents on the TPY scaffold plays a crucial role in modulating the electronic properties and overall photocatalytic efficiency of metal complexes. Alkoxy groups are known to be electron-donating, which significantly influences the electronic structure, charge distribution, and photophysical behavior of the TPY ligand. The findings reinforce the versatility of terpyridine-based metal complexes as effective and sustainable photocatalysts, offering substantial advancements in wastewater treatment, particularly for pharmaceutical pollutants. The synergistic effect of electronic tuning and structural modifications conferred by alkoxy groups underscores their importance in designing highly efficient TPY-based photocatalysts. These findings provide valuable insights for the rational development of next-generation metal complexes with superior performance in environmental remediation and wastewater treatment.

Henceforth, the newly synthesized complexes, especially **C5**, demonstrate superior photocatalytic performance compared to previously studied systems. Their remarkable degradation efficiency, favorable reaction kinetics, and excellent recyclability highlight their potential for real-world applications in environmental remediation. This study underscores the importance of electronic structure optimization in designing next-generation photocatalysts for the effective removal of persistent organic pollutants from aqueous systems.

4. Structure–property relationship

The photocatalytic activity of the synthesized metal complexes demonstrated a strong correlation with their structural characteristics, including the nature of the central metal, ligand type, and overall geometry (Fig. 5). The degradation efficiency of diclofenac (**DCF**) varied significantly among the complexes, following the order: **C5** (84.3%) > **C2** (81.5%) > **C4** (77.2%) > **C6** (72.6%) > **C1** (68.5%) > **C3** (64.1%).

The superior photocatalytic performance of **C5** can be attributed to the propoxy (–OPr) substituent, which provides minimal steric hindrance and facilitates greater substrate accessibility to the zinc center. Additionally, the electron-donating nature of the propoxy group strengthens the Zn–ligand bond, enhancing charge transfer efficiency. In contrast, **C2**, featuring a butoxy (–OBu) group, exhibited a slight reduction in efficiency due to the increased steric bulk, which weakens the Zn–ligand interaction and reduces electron transfer capacity. Similarly, the presence of a benzyloxy ($–OCH_2Ph$)

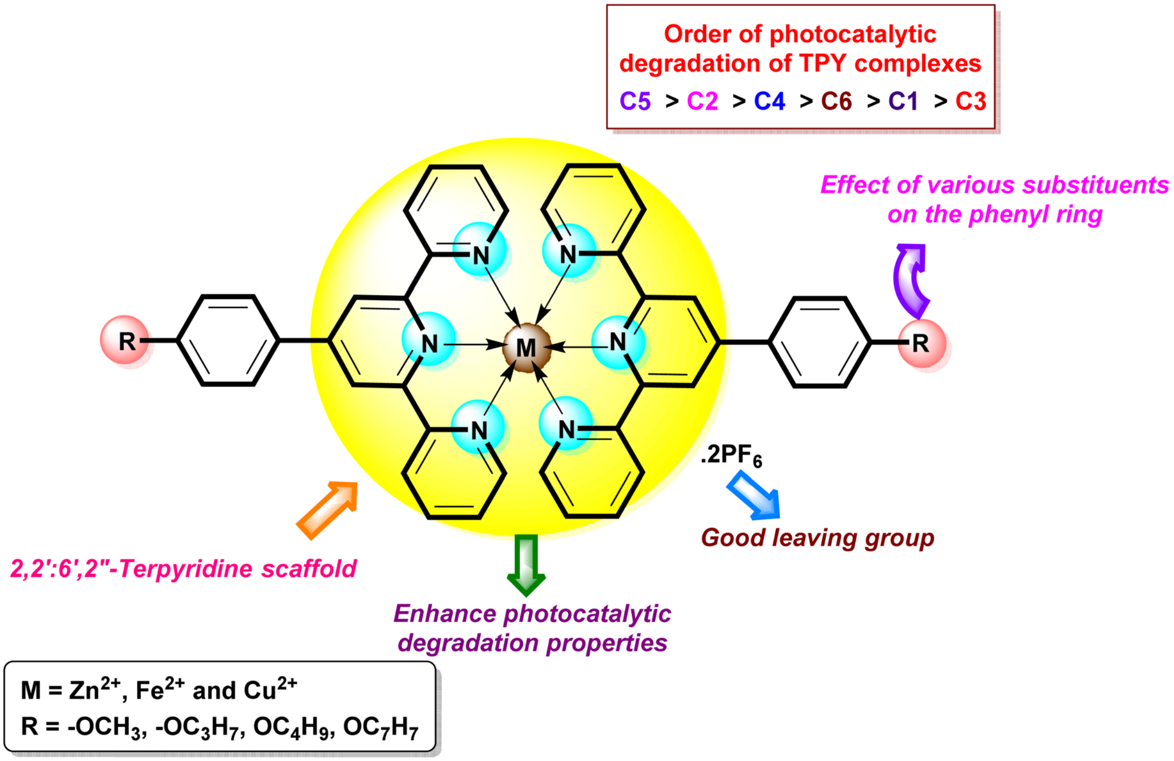

Fig. 5 Structure–property relationship of the target terpyridine-based complexes.

substituent in **C4** further diminished degradation efficiency, primarily due to the significant steric hindrance imposed by the bulky benzene ring. While benzyloxy groups possess electron-donating properties, their extensive delocalization reduces the electron density available for efficient catalytic activation.

Among the remaining complexes, **C6** (Cu complex) outperformed the Fe-based counterparts (**C1** and **C3**) due to the presence of dimethoxy (–OMe) substituents. These groups, being relatively small, introduce less steric hindrance while enhancing electron transfer through both inductive and resonance effects. The reduced catalytic activity of Fe complexes is attributed to their increased steric hindrance and lower ligand-field stabilization, which limits effective interaction with the substrate.

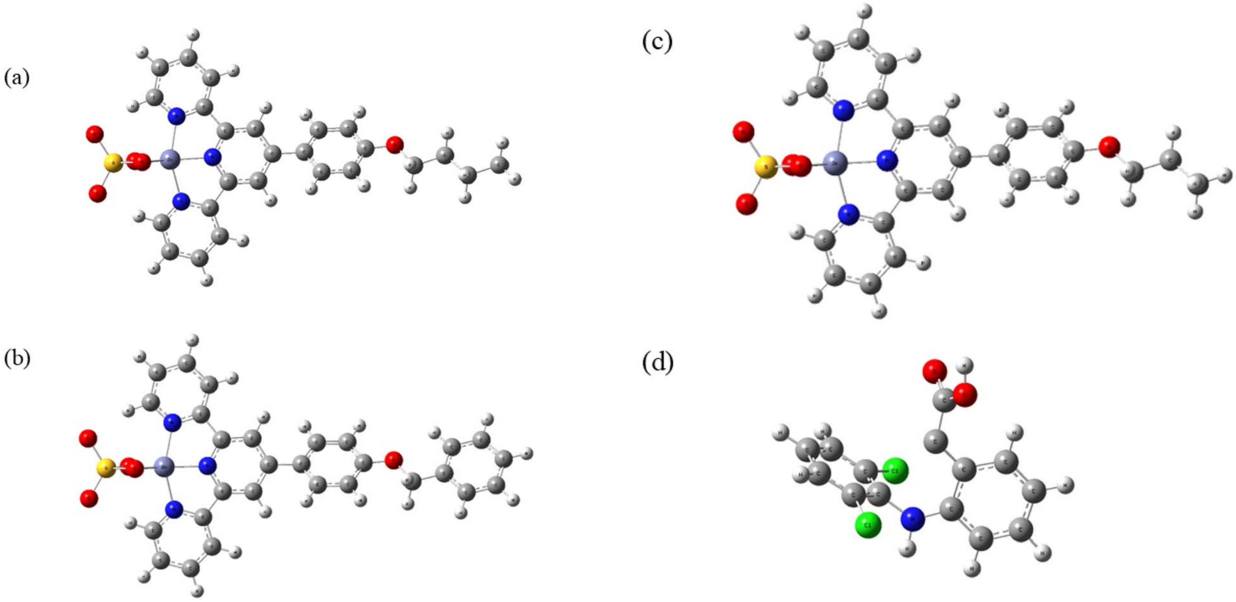

Fig. 6 The optimized structure of (a) C2, (b) C4, (c) C5 and (d) DCF.

The observed trend in photocatalytic efficiency can be further explained by the coordination number and geometry of the metal centers. Zinc complexes (**C2**, **C4**, **C5**) adopt a tetrahedral coordination, providing vacant sites that enhance pollutant adsorption and electron transfer. In contrast, Fe and Cu complexes (**C1**, **C3**, **C6**) exhibit octahedral coordination, where ligand saturation restricts substrate interaction, thereby lowering catalytic activity. This structural constraint inhibits efficient charge transfer from the metal center to the substrate, ultimately reducing photocatalytic performance.

Overall, the structure–property relationship highlights those steric effects, electronic properties, and coordination geometry play crucial roles in dictating the catalytic activity of these metal complexes. Zinc-based complexes, particularly those with small electron-donating substituents, exhibited superior photocatalytic efficiency, emphasizing the importance of rational ligand design in optimizing photocatalyst performance.

5. DFT studies

Fig. 6 and 7 illustrate the optimized structures of **C2**, **C4**, **C5**, and **DCF**, as well as the DOS for **C2**, **C4**, and **C5**, respectively. Fig. 6 demonstrates that there is no major alteration in the HOMO–LUMO gap.

Theoretical model widely utilized is MEP in catalyst chemistry to investigate possible areas for nucleophilic and electrophilic attacks on photocatalysts and pollutants using map of reactivity. Potential on the surface has been categorized into five distinct colors, in this manner: blue < green < yellow < orange < red. Fig. 8 illustrates that the deep red areas close to the atoms denote the locations of the highest chance for an electrophilic attack. The blue zone at the atoms indicates the probable sites for nucleophilic attack in the interaction between the photocatalysts and the pollutant. To explain the reaction process

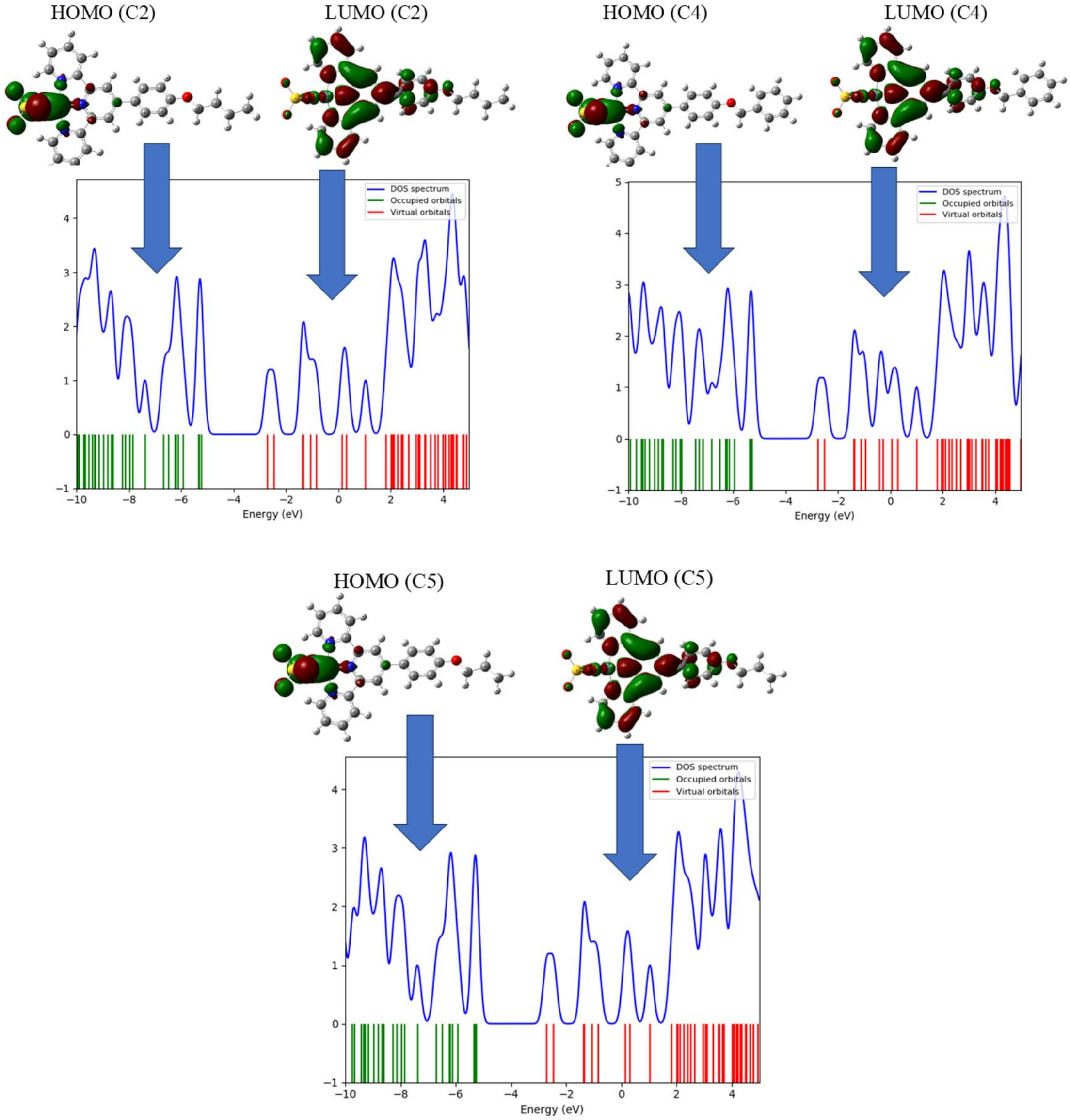

Fig. 7 The DOS and HOMO, LUMO of the **C2**, **C4** and **C5**.

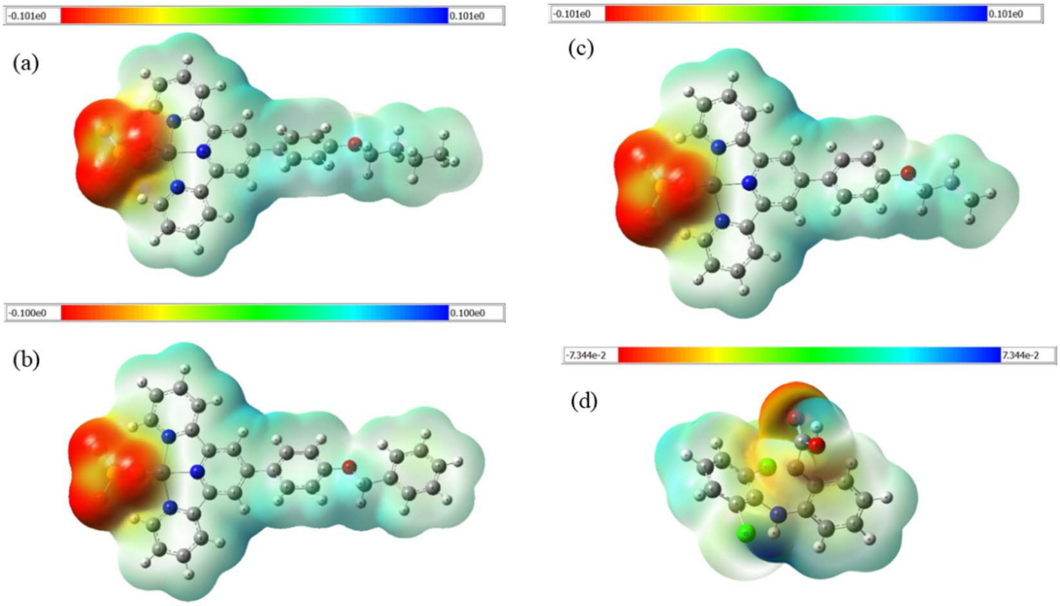

Fig. 8 The MEP of the (a) **C2**, (b) **C4**, (c) **C5** and (d) **DCF**.

Table 4 DFT calculation of quantum chemical parameters of **C2**, **C4**, **C5**, and **DCF**

Name	HOMO (eV)	LUMO (eV)	η (eV)	μ (eV)	σ (eV^{-1})	χ (eV)	LUMO–HOMO (eV)	ΔN (eV)
C2	−5.2357	−2.7083	1.2637	−3.9720	0.7913	3.972	2.5274	−12.485
C4	−5.2722	−2.7592	1.2563	−4.0157	0.7959	4.0157	2.5130	−12.839
C5	−5.2390	−2.7116	1.2637	−3.9753	0.7913	3.9753	2.5274	−12.505
DCF	−5.0365	−2.6906	1.1729	−3.8635	0.8526	3.8635	2.3459	−12.726

among the photocatalysts (**C2**, **C4**, **C5**) and **DCF**, descriptors were assessed in the subsequent section.

The reactivity descriptors of **C2**, **C4**, **C5**, and **DCF** were computed and analyzed to investigate the correlation among structure, stability, and chemical reactivity. The difference between HOMO–LUMO is a reliable predictor of the non-covalent interaction between photocatalysts and reactants.[75] The energy difference between HOMO–LUMO is a crucial characteristic for comparing the reactivity of **C2**, **C4**, and **C5** with respect to **DCF**. A smaller gap corresponds to increased reactivity among the photocatalysts.

According to the difference between HOMO–LUMO presented in Table 4, the photocatalysts reactivity and **DCF** may be ordered as follows: **DCF** (2.3459 eV) < **C2** = **C5** (2.5274 eV) ≈ **C4** (2.5130 eV). According to the values, during the photodegradation of **DCF** utilizing **C2**, **C4**, and **C5** as photocatalysts. **C2**, **C4**, and **C5** function as nucleophiles, while **DCF** acts as an electrophile.[76]

Some important reactivity parameters such as chemical hardness(η), chemical potential (μ), electronegativity (χ), and softness (σ). The compounds' reactivity and chemical stability were assessed using absolute hardness (η) and softness (σ). A lower value of η correlates with increased reactivity among the chemicals. In this investigation, **C2**, **C4**, and **C5** exhibit almost equivalent values (1.255 eV). The results corresponded with the computed difference between HOMO–LUMO, indicating that photocatalysts with a smaller difference between HOMO–LUMO exhibit the greatest η, suggesting that the compound has the tendency to donate electrons to an acceptor during the process. The highest charge transfers ($\Delta N_{\max}$) for **DCF** (−12.726 eV), **C2** (−12.485 eV), **C4** (−12.839 eV), and **C5** (−12.505 eV) were computed using eqn (4).

According to the data observed from eqn (5), **DCF** experiences electrophilic nucleophilic and nucleophilic attacks when interacting with **C2**, **C4**, and **C5**, respectively. The electrophilic charge transfer (ECT) was calculated using eqn (5). The ECT values for the **DCF–C2** (0.241 eV) and **DCF–C5** (0.221 eV) complexes are positive, whereas the value for the **DCF–C4** complex (−0.113 eV) is negative. According to this study, **C2**, **C4** and **C5** engage in nucleophilic and electrophilic substitution by either giving or accepting an electron from **DCF**, therefore establishing a non-covalent contact.[75,76]

$$\Delta N = \frac{-\mu^2}{\eta} \tag{4}$$

$$\mathrm{ECT} = \left(\Delta N_{\max(\mathbf{DCF})}\right) - \left(\Delta N_{\max(\mathbf{C2}\ \text{or}\ \mathbf{C4}\ \text{or}\ \mathbf{C5})}\right) \tag{5}$$

The HOMO and LUMO indicate the molecular chemical stability, with red indicating negative charge and green

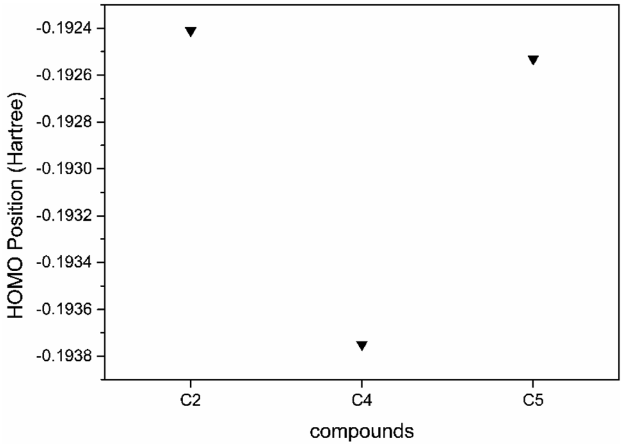

Fig. 9 HOMO positioning of **C2**, **C4**, and **C5** compounds.

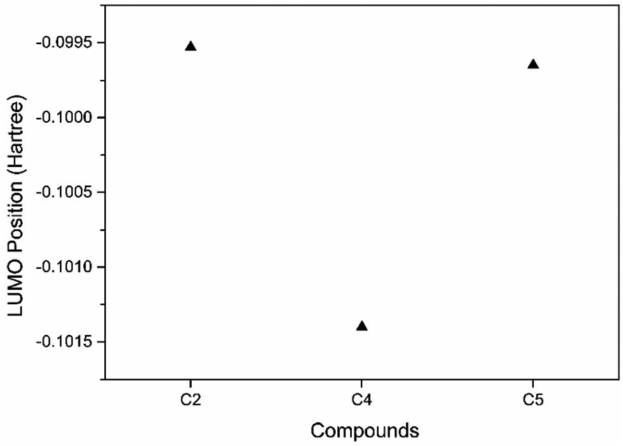

Fig. 10 LUMO positioning of **C2**, **C4**, and **C5** compounds.

signifying positive charges associated with the compound. The HOMO and LUMO denote the electron donor and electron acceptor, respectively. Fig. 7 indicates that the HOMO and LUMO electron densities of all the catalysts exhibit small variations.

The results for the HOMO of the compound studied are shown in Fig. 9, and the LUMO of the compound studied is shown in Fig. 10. The main contributors to degradation were hydroxyl radicals ($OH^{\bullet}$) and superoxide radical anion ($^{\bullet}O_2^-$). The HOMO and LUMO positioning are responsible for $OH^{\bullet}$ and ($^{\bullet}O_2^-$) respectively.[77] The HOMO position is more negative, representing more $OH^{\bullet}$ contributors, and if LUMO is more positive, it represents more ($^{\bullet}O_2^-$) contributors. From Fig. 8 and 9 we can say that **C5** has more $OH^{\bullet}$ contributors than **C2** and more ($^{\bullet}O_2^-$) contributors than **C4**. From here, we can say that both contributors make **C5** the most efficient compound for degradation.

Fig. 11 illustrates the formation energy of various compounds, revealing that **C5** has a higher energy than **C2** and **C4**, which could potentially account for its high degradation efficiency. High energy means less stability, which increases the tendency of a compound to interact with a pollutant for degradation. The HOMO–LUMO gaps of **C2**, **C4**, and **C5** were found to be similar at 2.52 eV with a difference of ±0.01 eV. These minor differences in the energy gaps can be attributed to the synthesis methods used.

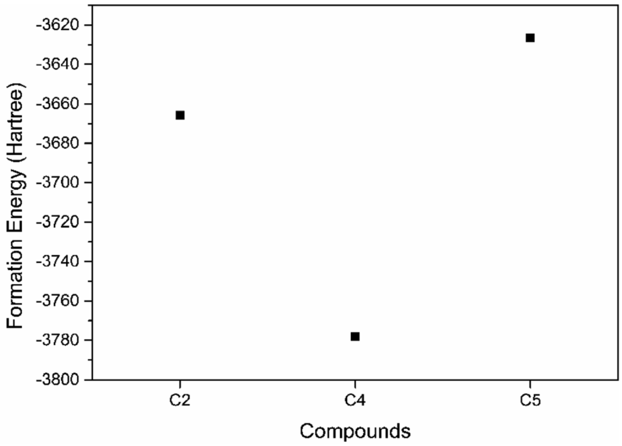

Fig. 11 Formation energies of **C2**, **C4**, and **C5** compounds.

6. Conclusions

In summary, we have successfully accomplished the synthesis of the target complexes (**C1–C6**) with high yields, and their structural features were thoroughly characterized using various spectroscopic techniques (UV, IR, NMR and mass spectrometry). The synthesized complexes were employed in heterogeneous photocatalysis to degrade a water pollutant **DCF**. The findings of this study demonstrate a substantial advancement in the photocatalytic application of TPY-based metal complexes, particularly in the degradation of pharmaceutical pollutants such as diclofenac potassium, surpassing previous studies on methylene blue degradation by exhibiting higher efficiency, superior charge transfer characteristics, and excellent recyclability, thus establishing these novel alkoxy-functionalized TPY complexes as promising candidates for sustainable wastewater treatment technologies. The photocatalytic efficiencies of the complexes were in the order: **C5** (84.3%) > **C2** (81.5%) > **C4** (77.2%) > **C6** (72.6%) > **C1** (68.5%) > **C3** (64.1%). Among different complexes of transition metal with a TPY backbone, **C5** effectively removed 10 mg L^{-1} of **DCF**, achieving a degradation efficiency of 90.2% within 90 min of light irradiation employing only 20 mg of the catalyst at pH 5. The reaction kinetics was in accordance with the pseudo-first-order kinetics with the highest rate constant observed for **C5** at 0.02355 min^{-1} and the sustainable photocatalytic performance of **C5** up to four repeated cycles indicated its economic feasibility. The photocatalytic experiments carried out in the presence of scavengers revealed that the prime reactive species involved in the degradation process were $^{\bullet}O_2^-$ and $OH^{\bullet}$. Furthermore, the correlation between DFT results and experimental findings provides insight into the photocatalytic efficiencies of the studied complexes. The HOMO–LUMO gap analysis indicates that **C2**, **C4**, and **C5** exhibit similar reactivity (~2.52 eV). Additionally, the DOS study revealed that **C5** exhibits an improved photoactivity value owing to the enhanced localization and delocalization of the HOMO and LUMO in **C5** compared to **C2** and **C4**. The position of the HOMO and LUMO is responsible for $OH^{\bullet}$ and $(^{\bullet}O_2^{-})$, respectively, which makes **C5** a suitable option for photoactivity. According to the DFT calculation, the nucleophilic and electrophilic attacks occur during the formation of the **C2–DCF**, **C5–DCF**, and **C4–DCF** complexes, respectively. DFT results align with experimental findings, reinforcing the role of electronic structure in photocatalytic performance and highlighting computational methods as valuable tools for screening effective photocatalysts for environmental remediation. In conclusion, the **C5** is an efficient candidate for promising applications of rapid degradation **DCF** in pharmaceutical wastewater. However, the practical utility of this catalyst requires upscaled synthesis and photocatalytic studies employing real wastewater to assess its industrial feasibility. The catalyst should also be evaluated against other emerging contaminants, such as pesticides, microplastics, and various personal care products, to further broaden its environmental impact. Moreover, assessing the potential toxicity associated with this catalyst is crucial to ensure environmental regulatory standards. These future directions could significantly strengthen the applicability of TPY-based metal complexes for sustainable wastewater treatment.

Data availability

All the data is provided in the manuscript and ESI file.†

Author contributions

Ehsan Ullah Mughal: Main idea, supervision, methodology, final writing the manuscript. Nafeesa Naeem: Data analysis and collection, reviewing, editing, first-draft preparation. Farwa Zainab: Experimental work performance. Ayesha Javaid: Performed photodegradation studies, first-draft preparation. Muhammad Imran: Methodology, performed photodegradation studies. Sujeet Kumar Pandey: Computational studies. Amina Sadiq: Formal analysis. Ayza Jabeen: Formal analysis. Hanan A. Ogaly: Formal analysis. Fatimah AM Al-Zahrani: Formal analysis. Abdullah Yahya Abdullah Alzahrani: Formal analysis. All authors gave final approval for publication.

Conflicts of interest

No conflict of interest to declare.

Acknowledgements

The authors extend their appreciation to the Deanship of Research and Graduate Studies at King Khalid University for funding this work through Large Research Project under grant number RGP2/152/45.

References

1 K. P. Garnock-Jones, *CNS Drugs*, 2014, **28**, 761–768.
2 B. Chuasuwan, V. Binjesoh, J. Polli, H. Zhang, G. Amidon, H. Junginger, K. Midha, V. Shah, S. Stavchansky and J. Dressman, *J. Pharm. Sci.*, 2009, **98**, 1206–1219.
3 A. Saylan, C. A. Turel, I. Turel, A. Cetinkaya, I. E. Torun and H. Celik, *Exp. Biomed. Res.*, 2023, **6**, 77–87.
4 H. Mabrouki and D. Akretche, *Desalin. Water Treat.*, 2016, **57**, 6033–6043.
5 S. Chime, A. Attama, F. Kenechukwu, E. Umeyor and G. Onunkwo, *Br. J. Pharm. Res.*, 2013, **3**, 90.
6 I. Alessandretti, C. V. T. Rigueto, M. T. Nazari, M. Rosseto and A. Dettmer, *J. Environ. Chem. Eng.*, 2021, **9**, 106743.
7 A. C. F. P. Fuhr, C. F. de Azevedo, N. Ahmad, S. Mohandoss, G. L. Dotto and F. M. Machado, *J. Mol. Liq.*, 2024, **407**, 125191.
8 R. Wang, Z. Wang, H. Yuan, C. Li and N. Zhu, *J. Hazard. Mater.*, 2024, **479**, 135603.
9 L. Lonappan, S. K. Brar, R. K. Das, M. Verma and R. Y. Surampalli, *Environ. Int.*, 2016, **96**, 127–138.
10 K. Onwuka, C. F. Aaron, C. I. Nosiri, O. C. Atasie, C. Aguwamba and N. I. Uzoamaka, *JCNB*, 2024, **5**, 37–55.
11 J. M. Angosto, M. J. Roca and J. A. Fernández-López, *Water*, 2020, **12**, 3567.
12 F.-P. Huang, W.-J. Qin, X.-Y. Pan, K. Yang, K. Wang and Q.-H. Teng, *J. Org. Chem.*, 2024, **89**, 4395–4405.
13 N. S. dos Santos, L. F. Marquiza, C. S. C. Calheiros, P. S. Cavalheri, B. S. Machado, G. H. Cavazzana and F. J. C. M. Filho, *Water*, 2021, **13**, 1043.
14 C. F. de Azevedo, N. F. de Souza, F. B. Cardoso, A. C. F. P. Fuhr, E. C. Lima, A. G. Osório and F. Machado Machado, *Environ. Sci. Pollut. Res.*, 2024, **31**, 48650–48662.
15 X. Yang, J. Yang, T. Zhao, W. Qian, Y. Wang, A. Holmen, W. Jiang, D. Chen and H. Ben, *Chem. Eng. J.*, 2022, **445**, 136655.
16 A. Javaid, M. Imran, F. Kanwal and S. Latif, *Mater. Sci. Semicond. Process.*, 2024, **177**, 108350.
17 N. Zhang, J. Li, G. Liu, X. Chen and K. Jiang, *Water Sci. Technol.*, 2017, **75**, 2163–2170.
18 S. K. Srivastava, *RSC Appl. Interfaces*, 2024, **1**(3), 340–429.
19 K. Prakruthi, M. P. Ujwal, S. R. Yashas, B. Mahesh, N. Kumara Swamy and H. P. Shivaraju, *Environ. Sci. Pollut. Res.*, 2022, **29**, 4930–4957.
20 A. Javaid, M. Imran, F. Kanwal, S. Latif, S. F. Adil, M. R. Shaik and M. Khan, *Molecules*, 2023, **28**, 7979.
21 G.-R. Wu, J.-K. Xu, L.-J. Sun, Y.-F. Li, S.-Q. Gao and Y.-W. Lin, *J. Environ. Chem. Eng.*, 2023, **11**, 111471.
22 A. Intisar, A. Ramzan, S. Hafeez, N. Hussain, M. Irfan, N. Shakeel, K. A. Gill, A. Iqbal, M. Janczarek and T. Jesionowski, *Chemosphere*, 2023, **336**, 139203.
23 G. Amariei, K. Boltes, R. Rosal and P. Leton, *PLoS One*, 2020, **15**, e0227267.
24 I. Tbessi, M. Benito, J. Llorca, E. Molins, S. Sayadi and W. Najjar, *J. Alloys Compd.*, 2019, **779**, 314–325.

25 A. B. Ganganboina, M. D. Nguyen, T. H. L. Nguyen, E. P. Kuncoro and R.-A. Doong, *Chem. Eng. J.*, 2021, **425**, 131520.
26 W. Liu, Y. Li, F. Liu, W. Jiang, D. Zhang and J. Liang, *Water Res.*, 2019, **151**, 8–19.
27 S. Li, J. Cui, X. Wu, X. Zhang, Q. Hu and X. Hou, *J. Hazard. Mater.*, 2019, **373**, 408–416.
28 A. Tufail, S. Alharbi, J. Alrifai, A. Ansari, W. E. Price and F. I. Hai, *Process Saf. Environ. Prot.*, 2021, **145**, 110–119.
29 F. T. Geldasa, M. A. Kebede, M. W. Shura and F. G. Hone, *RSC Adv.*, 2023, **13**, 18404–18442.
30 X. Liu, F. Li, Y. Liu, P. Li, L. Chen, B. Li, T. Qian and W. Liu, *J. Environ. Chem. Eng.*, 2022, **10**, 107545.
31 T. Velempini, E. Prabakaran and K. Pillay, *Mater. Today Chem.*, 2021, **19**, 100380.
32 V. Calisto, M. R. M. Domingues and V. I. Esteves, *Water Res.*, 2011, **45**, 6097–6106.
33 S. Kothawade and P. Shende, *Coord. Chem. Rev.*, 2024, **510**, 215851.
34 E. U. Mughal, S. F. Kainat, N. Naeem, M. Imran, A. Javaid, A. Sadiq, A. Y. A. Alzahrani, S. B. Moussa and S. A. Ahmed, *Dyes Pigm.*, 2024, 112254.
35 E. U. Mughal, A. Javaid, M. Imran, M. A. Abourehab, E. B. Elkaeed, N. Naeem, A. Y. A. Alzahrani, A. Sadiq and S. F. Kainat, *Inorg. Chim. Acta*, 2023, **546**, 121329.
36 C. Wei, Y. He, X. Shi and Z. Song, *Coord. Chem. Rev.*, 2019, **385**, 1–19.
37 A. Winter and U. S. Schubert, *ChemCatChem*, 2020, **12**, 2890–2941.
38 S. F. Kainat, M. B. Hawsawi, E. U. Mughal, N. Naeem, A. M. Almohyawi, H. M. Altass, E. M. Hussein, A. Sadiq, Z. Moussa and A. S. Abd-El-Aziz, *RSC Adv.*, 2024, **14**, 21464–21537.
39 Y. Wang, T. Liu, L. Chen and D. Chao, *Inorg. Chem.*, 2021, **60**, 5590–5597.
40 D. Saccone, C. Magistris, N. Barbero, P. Quagliotto, C. Barolo and G. Viscardi, *Materials*, 2016, **9**, 137.
41 K. Liu, L. Du and T. Wang, *Inorg. Chem.*, 2024, **63**, 4614–4627.
42 E. U. Mughal, R. J. Obaid, A. Sadiq, M. A. Alsharif, N. Naeem, S. Kausar, A. A. Altaf, R. S. Jassas, S. Ahmed and R. I. Alsantali, *Dyes Pigm.*, 2022, **201**, 110248.
43 X. Sun, H. D. Cole, G. Shi, V. Oas, A. Talgatov, C. G. Cameron, S. Kilina, S. A. McFarland and W. Sun, *Inorg. Chem.*, 2024, **63**, 21323–21335.
44 E. U. Mughal, M. Mirzaei, A. Sadiq, S. Fatima, A. Naseem, N. Naeem, N. Fatima, S. Kausar, A. A. Altaf and M. N. Zafar, *R. Soc. Open Sci.*, 2020, **7**, 201208.
45 V. Barone, J. Bloino and M. Biczysko, *Vibrationally-resolved electronic spectra in GAUSSIAN 09. Revision a, 2(1)*, 2009, pp. 1–20.
46 M. Frisch and F. Clemente, G. Scalmani, V. Barone, B. Mennucci, G. A. Petersson, H. Nakatsuji, M. Caricato, X. Li, H. P. Hratchian, A. F. Izmaylov, J. Bloino and G. Zhe, *Gaussian, 9*.
47 R. Dennington, T. A. Keith and J. M. Millam, *GaussView 6.0.16*, Semichem Inc., Shawnee Mission, KS, USA, 2016, pp. 143–150.
48 N. Chakinala, P. Ranjan, A. G. Chakinala and P. R. Gogate, *Catal. Commun.*, 2023, **174**, 106589.
49 G. Wu, Y. Liu, G. Liu, R. Hu and G. Gao, *J. Mol. Liq.*, 2021, **328**, 115411.
50 A. Akbari, Z. Sabouri, H. A. Hosseini, A. Hashemzadeh, M. Khatami and M. Darroudi, *Inorg. Chem. Commun.*, 2020, **115**, 107867.
51 C. Paraschiv, A. Cucos, S. Shova, A. M. Madalan, C. Maxim, D. Visinescu, B. Cojocaru, V. I. Parvulescu and M. Andruh, *Cryst. Growth Des.*, 2015, **15**, 799–811.
52 S. Ranjan Jena, T. Mandal and J. Choudhury, *Chem. Rec.*, 2022, **22**, e202200165.
53 M. Hernick and C. Fierke, *Comprehensive Natural Products II*, 2010, vol. 8, pp. 547–581.
54 S. Wang, Z. Liu, Y. Zhao, W. Song, Z. Sun and J. Ma, *J. Environ. Chem. Eng.*, 2024, **12**, 113087.
55 Z. Xiao, W. Yang, J. Wang, S. Cao, J. Yang and M. Zhu, *Chem. Eng. J.*, 2025, **504**, 159022.
56 F. Han, X. Ye, Q. Chen, H. Long and Y. Rao, *Sep. Purif. Technol.*, 2020, **232**, 115967.
57 M. A. Behnajady, H. Eskandarloo, N. Modirshahla and M. Shokri, *Dig. J. Nanomater. Biostructures*, 2011, **6**, 1887–1895.
58 A. Javaid, M. Imran, M. P. Rayaroth, X. Sun, C. Wang, G. Boczkaj and M. Momotko, *Curr. Opin. Chem. Eng.*, 2024, **46**, 101054.
59 P. John, K. Johari, N. Gnanasundaram, A. Appusamy and M. Thanabalan, *Environ. Technol. Innovation*, 2021, **22**, 101412.
60 K. V. Plakas, V. C. Sarasidis, S. I. Patsios, D. A. Lambropoulou and A. J. Karabelas, *Chem. Eng. J.*, 2016, **304**, 335–343.
61 N. Ahmadpour, M. H. Sayadi, S. Sobhani and M. Hajiani, *J. Environ. Manage.*, 2020, **271**, 110964.
62 L. Rueda-Salaya, A. Hernández-Ramírez, L. Hinojosa-Reyes, J. Guzmán-Mar, M. Villanueva-Rodríguez and E. Sánchez-Cervantes, *J. Photochem. Photobiol., A*, 2020, **391**, 112364.
63 L. Gao, B. Zhou, F. Wang, R. Yuan, H. Chen and X. Han, *Environ. Sci. Pollut. Res.*, 2020, **27**, 2044–2053.
64 N. Aghababaei, M. Abdouss, H. Hosseini-Monfared and F. Ghanbari, *J. Environ. Chem. Eng.*, 2023, **11**, 110477.
65 Z. Wu, J. Liu, J. Shi and H. Deng, *Environ. Res.*, 2024, **249**, 118361.
66 A. Javaid, M. Imran, F. Kanwal, S. Latif, M. Khan, M. Kuniyil, M. R. Shaik, M. R. H. Siddiqui and S. F. Adil, *Ceram. Int.*, 2024, **50**, 41915–41930.
67 A. Javaid, M. Imran, F. Kanwal, S. Latif and M. N. Khan, *J. Water Process Eng.*, 2025, **69**, 106665.
68 S.-Q. Li, M. Ray, A.-J. Zhu, X. Zhang, A. K. Pradhan, A. Mohanty, M. Muddassir and J.-C. Jin, *Polyhedron*, 2024, **262**, 117166.
69 Y. Wen, M. Feng, P. Zhang, H.-C. Zhou, V. K. Sharma and X. Ma, *ACS ES&T Eng.*, 2021, **1**, 804–826.
70 V. Muelas-Ramos, M. Sampaio, C. Silva, J. Bedia, J. Rodriguez, J. Faria and C. Belver, *J. Hazard. Mater.*, 2021, **416**, 126199.
71 K. Hemkumar, P. Ananthi and A. Pius, *Mater. Sci. Eng., B*, 2023, **292**, 116453.

72 D. Pourkodee, D. R. Devee and E. Sailatha, *Inorg. Chem. Commun.*, 2024, 113585.

73 N. Aghababaei, M. Abdouss, H. Hosseini-Monfared and F. Ghanbari, *J. Water Process Eng.*, 2023, **53**, 103702.

74 G. Tseberlidis, V. Trifiletti, A. H. Husien, A. L'Altrella, S. Binetti and F. Gosetti, *Appl. Sci.*, 2024, **14**, 9923.

75 J. Sharma, I. Mishra and V. Kumar, *J. Environ. Manage.*, 2016, **166**, 12–22.

76 F. B. Shittu, A. Iqbal, M. N. Ahmad, M. R. Yusop, M. N. M. Ibrahim, S. Sabar, L. D. Wilson and D. H. Y. Yanto, *RSC Adv.*, 2022, **12**, 10409–10423.

77 S. Kaya and C. Kaya, *Comput. Theor. Chem.*, 2015, **1060**, 66–70.